AGU PUBLICATIONS

JGR

Journal of Geophysical Research: Atmospheres

RESEARCH ARTICLE

10.1002/2013JD020035

Key Points:
- About 50% of cirrus occurrences at ARM SGP is explained by three synoptic conditions
- Cirrus microphysics exhibit striking differences among synoptic regimes
- Vertical velocity is a poor predictor of cirrus microphysical variability

Correspondence to:
A. Muhlbauer,
andreasm@atmos.washington.edu

Citation:
Muhlbauer, A., T. P. Ackerman, J. M. Comstock, G. S. Diskin, S. M. Evans, R. P. Lawson, and R. T. Marchand (2014), Impact of large-scale dynamics on the microphysical properties of midlatitude cirrus, *J. Geophys. Res. Atmos.*, *119*, 3976–3996, doi:10.1002/2013JD020035.

Received 16 APR 2013
Accepted 11 MAR 2014
Accepted article online 15 MAR 2014
Published online 2 APR 2014

Impact of large-scale dynamics on the microphysical properties of midlatitude cirrus

Andreas Muhlbauer[1], Thomas P. Ackerman[1,2], Jennifer M. Comstock[3], Glenn S. Diskin[4], Stuart M. Evans[2], R. Paul Lawson[5], and Roger T. Marchand[2]

[1]Joint Institute for the Study of the Atmosphere and Ocean, University of Washington, Seattle, Washington, USA, [2]Department of Atmospheric Sciences, University of Washington, Washington, USA, [3]Pacific Northwest National Laboratory, Richland, Washington, USA, [4]NASA Langley Research Center, Hampton, Virginia, USA, [5]Spec Inc., Boulder, Colorado, USA

Abstract In situ microphysical observations of midlatitude cirrus collected during the Department of Energy Small Particles in Cirrus (SPARTICUS) field campaign are combined with an atmospheric state classification for the Atmospheric Radiation Measurement (ARM) Southern Great Plains (SGP) site to understand statistical relationships between cirrus microphysics and the large-scale meteorology. The atmospheric state classification is informed about the large-scale meteorology and state of cloudiness at the ARM SGP site by combining ECMWF ERA-Interim reanalysis data with 14 years of continuous observations from the millimeter-wavelength cloud radar. Almost half of the cirrus cloud occurrences in the vicinity of the ARM SGP site during SPARTICUS can be explained by three distinct synoptic conditions, namely, upper level ridges, midlatitude cyclones with frontal systems, and subtropical flows. Probability density functions (PDFs) of cirrus microphysical properties such as particle size distributions (PSDs), ice number concentrations, and ice water content (IWC) are examined and exhibit striking differences among the different synoptic regimes. Generally, narrower PSDs with lower IWC but higher ice number concentrations are found in cirrus sampled in upper level ridges, whereas cirrus sampled in subtropical flows, fronts, and aged anvils show broader PSDs with considerably lower ice number concentrations but higher IWC. Despite striking contrasts in the cirrus microphysics for different large-scale environments, the PDFs of vertical velocity are not different, suggesting that vertical velocity PDFs are a poor predictor for explaining the microphysical variability in cirrus. Instead, cirrus microphysical contrasts may be driven by differences in ice supersaturations or aerosols.

1. Introduction

Cirrus clouds contribute about 30% to the global high cloud cover but exhibit pronounced latitudinal variability ranging from 20% in midlatitude storm tracks to more than 50% in the Tropics [*Stubenrauch et al.*, 2006; *Sassen et al.*, 2008]. Cirrus clouds have a strong impact on the radiative energy balance of the Earth by reflecting parts of the incoming solar radiation back to space and absorbing and reemitting longwave radiation [*Ackerman et al.*, 1988]. Due to these two opposing radiative effects, the net radiative forcing of cirrus clouds can be positive or negative depending on the cirrus radiative properties. The radiative properties of cirrus are in turn controlled by cirrus microphysical (e.g., crystal habits, particle size distribution, and ice water content) and macrophysical properties (e.g., cloud height, geometrical thickness, cloud fraction, and cloud lifetime).

Recent studies show that cirrus clouds are the dominant contributor to the longwave cloud feedback in Global Climate Models (GCMs) [*Zelinka et al.*, 2012], but uncertainties remain regarding the magnitude of the cirrus cloud forcing and its role for climate sensitivity. These uncertainties are largely tied to deficiencies in representing the observed spatiotemporal variability of cirrus in GCMs. Perturbed physics ensemble experiments with GCMs suggest that one of the leading factors contributing to the spread in climate sensitivity among GCMs is ice terminal fall velocities that control the ice water path (IWP) and cirrus cloud cover in the simulations [*Sanderson et al.*, 2008]. Furthermore, assumptions about the particle size distribution (PSD) in cirrus and, in particular, the contributions from small (maximum dimension smaller than 50 μm) ice crystals to the total ice number concentrations are shown to have profound impacts on the IWP and radiative forcing exerted by cirrus [*Mitchell et al.*, 2008].

A fundamental problem for parameterizing cirrus in GCMs is the diversity of environmental conditions under which cirrus clouds form and the profound impacts these environmental conditions can have on the microphysical evolution and the life cycle of cirrus. Predicting the evolution of cirrus requires a priori knowledge of complex physical and dynamical processes operating on a wide range of scales. For example, past observations document midlatitude cirrus clouds forming in regions of large-scale and mesoscale uplift such as low pressure systems and fronts [*Sassen*, 1997], in the vicinity of warm conveyor belts [*Spichtinger et al.*, 2005a], breaking Rossby waves [*Eixmann et al.*, 2010], and in regions of strong upper level divergence and ageostrophic motion typically found in the vicinity of jet streaks [*Mace et al.*, 1995]. Furthermore, cirrus cloud formation can be triggered by mesoscale perturbations such as mountain waves [*Karcher and Strom*, 2003], internal waves near jet streams [*Spichtinger et al.*, 2005b], or deep convection [*Garrett et al.*, 2004]. Unfortunately, many of the important mesoscale dynamical processes cannot be explicitly resolved by current GCMs and, thus, require parameterization. Consequently, GCMs have considerable difficulty in representing cirrus microphysical and macrophysical properties and are unable to capture the mesoscale variability of cirrus induced by these different dynamical processes [*Liu et al.*, 2007; *Joos et al.*, 2008; *Gettelman et al.*, 2010]. A better understanding of the interactions among cirrus microphysics, macrophysics, and dynamics is important for advancing our fundamental understanding of cirrus cloud formation and life cycles and is a necessary step toward improving the representation of cirrus in GCMs and adding confidence to estimates of the climatic impact of cirrus. The core objective of this paper is to establish a clearer understanding of the relationship between the large-scale dynamical and thermodynamical structure of the atmosphere and the microphysical and macrophysical properties of cirrus clouds at midlatitudes. In order to achieve this goal, we combine meteorological reanalysis data from the European Center for Medium-Range Weather Forecasts (ECMWF) with radar backscatter measurements from the millimeter-wavelength cloud radar (MMCR) at the Southern Great Plains (SGP) site of the Atmospheric Radiation Measurement (ARM) Program and several months of in situ aircraft observations obtained during the recent U. S. Department of Energy (DOE) Small Particles in Cirrus (SPARTICUS) field campaign.

Section 2 of this paper introduces an objective atmospheric state classification scheme used to describe the large-scale characteristics of the atmosphere and discusses the statistical relationships to the observed cloudiness at the ARM SGP site by means of cluster analysis. The meteorology and statistics of atmospheric conditions leading to cirrus clouds during SPARTICUS are discussed in section 3. Section 4 details the in situ aircraft observations used throughout the study. Section 5 describes the contrasting characteristics of cirrus microphysical and macrophysical properties observed during SPARTICUS and relates the cirrus properties to the environmental conditions under which they form. The conclusions are presented in section 6.

2. Method

The objective classification of atmospheric states at the ARM SGP site is based on previous work by *Marchand et al.* [2006, 2009] and *Evans et al.* [2012], and only some fundamental aspects of the classification scheme are reviewed here to elucidate the concepts and limitations of this study. Atmospheric state classification methods are essentially clustering techniques used to relate similar patterns of cloud properties to meteorology in a statistically meaningful way. Various clustering techniques have been used in the past and are becoming increasingly popular as a tool to better understand statistical relationships between clouds and dynamics [e.g., *Evans et al.*, 2012; *Muelmenstaedt et al.*, 2012; *Berry and Mace*, 2013]. In this study the atmospheric state classification is based on a competitive neural network that objectively identifies and categorizes weather patterns and their associated state of cloudiness at the ARM SGP site. The neural network algorithm is informed about the large-scale environmental conditions of the atmosphere and cloud occurrence profiles by utilizing two independent data sets. The first data set is the ECMWF ERA-Interim reanalysis [*Dee et al.*, 2011] and is used to provide a best estimate of the meteorology at and around the ARM SGP site. The second data set provides long-term continuous observations of vertical hydrometeor occurrence profiles from ground-based MMCR reflectivity observations at the ARM SGP site [*Clothiaux et al.*, 2000].

The meteorological input to the neural network classifier consists of six hourly reanalysis fields of temperature, relative humidity, horizontal wind components, and surface pressure taken from the ECMWF ERA-Interim reanalysis for a 14 year period from 1996 to 2010. Each input field is defined on a 9×9 horizontal grid points centered at the ARM SGP site with a grid spacing of 1.5° and seven predefined pressure levels. Thus, at each time step (i.e., every 6 h) the neural network is provided with one meteorological observation that is an input vector with 2349 elements. The output of the neural network algorithm is a set of clusters,

Table 1. Basic Meteorological Characteristics of the Atmospheric States[a]

State	375 hPa Winds	500 hPa Winds	875 hPa Winds	375 hPa Relative Humidity	Surface Temperature
1	NW	NW	Anticyclonic	Dry	Cold
2	NW	NW	N, divergent	Dry	Warm
3	NW	NW	Anticyclonic	Dry	Warm
4	W, anticyclonic	SW	SW	Dry	Warm
5	SW	SW	SE	Moist	Cold
6	NW	NW	NW	Dry	Cold
7	NW	NW	Anticyclonic	Dry	Warm
8	SW	SW	S	Moist	Warm
9	SW	W	S	Moist	Warm
10	W	W	SW	Dry	Warm
11	W	W, convergent	S	Dry	Warm
12	SW	SW	SW, convergent	Moist	Cold
13	W	W	Anticyclonic	Moist	Cold
14	SW, cyclonic	W, cyclonic	N	Moist	Cold
15	W, anticyclonic	W, anticyclonic	SW	Dry	Warm
16	W	W	N, divergent	Moist	Cold
17	W	W	SW, convergent	Moist	Cold
18	SW, cyclonic	SW, cyclonic	Cyclonic	Dry	Cold
19	NW, cyclonic	NW, cyclonic	NW	Dry	Cold
20	SW	SW	SW, convergent	Dry	Warm
21	NW	NW	NW	Dry	Cold

[a]Winds at 375 hPa, 500 hPa, and 875 hPa, relative humidity at 375 hPa, and surface temperature are diagnosed from ECMWF ERA-Interim reanalysis fields. Wind directions are northerly (N), northwesterly (NW), westerly (W), southwesterly (SW), southerly (S), and southwesterly (SE). Cyclonic, anticyclonic, convergent, and divergent flow patterns are indicated as appropriate. Wet/dry conditions are defined as above/below 50% based on averaged relative humidities in the vicinity of the ARM SGP site. Warm/cold states are defined as above/below 10 °*C* based on averaged surface temperatures in the vicinity of the ARM SGP site.

each representing a certain atmospheric state in the vicinity of the ARM SGP site. Throughout this study we refer to an atmospheric state or cluster as a number of reoccurring similar weather patterns and we use these terminologies interchangeably. Each atmospheric state is characterized by environmental conditions with similar dynamical and thermodynamical properties as well as similar vertical cloud occurrence profiles. All clusters are statistically distinct from each other in terms of their meteorology and cloudiness over the ARM SGP site.

Due to the nature of the algorithm, the initial number of atmospheric states must be prescribed. We then perform an iterative procedure until the algorithm converges on a final set of states. Convergence is achieved by continuing the iterative procedure until all clusters are temporally stable and statistically distinct in terms of the mean cloud occurrence profile seen by the MMCR. For each state, temporal stability is achieved by comparing the mean hydrometeor occurrence profile in the first half of the record with that from the second half of the record and applying a statistical hypothesis test based on moving-blocks bootstrap resampling [*Marchand et al.*, 2006]. If the statistics test fails, meaning the radar profile of cloud occurrence is changing over time, the state is either divided, thereby increasing the total number of states, or eliminated, thereby reducing the total number of states. The decision whether a state is divided or removed depends on whether the total number of observations in the particular cluster exceeds a threshold criterion as detailed in *Evans et al.* [2012]. In a similar fashion, statistical distinctness in terms of cloudiness is achieved by applying the same hypothesis test to the hydrometeor occurrence profile in each state against all other states. Again, states failing the distinctness test are either divided or eliminated. Using this classification technique, *Marchand et al.* [2009] found overall 11 atmospheric states for the ARM SGP site based on 17 months of Rapid Update Cycle (RUC) analyses. This study finds 21 states using ECMWF's ERA-Interim reanalyses for a 14 year period (1996–2010). The discrepancy between these studies in terms of the total number of states can be explained by the number of observations that go into the cluster analysis. Increasing the number of observations generally allows for a finer partitioning of the cluster space and, thus, tends to increase the number of robust clusters. Sensitivity tests performed by *Evans et al.* [2012] suggest that changing the input variables, domain size, and horizontal resolution only marginally affects the results of the cluster analysis or the total number of clusters.

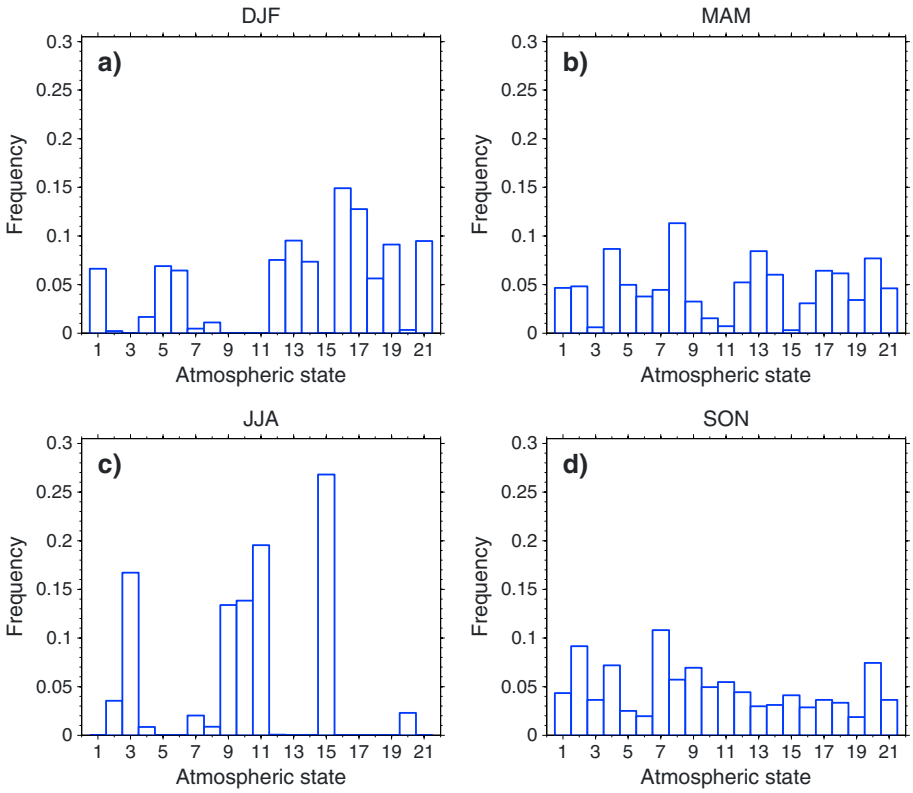

Figure 1. Distribution of the frequency of occurrence of atmospheric states at the ARM SGP site during (a) winter, (b) spring, (c) summer, and (d) fall. Data are based on the ECMWF ERA-Interim reanalysis for the time period 1979–2010. The histogram is normalized such that the sum of all occurrences equals unity.

Throughout this study, the 14 year atmospheric state classification is used as a tool to identify and categorize synoptic-scale weather events during the SPARTICUS field campaign (January–June 2010) and as a basis for compositing aircraft observations by large-scale meteorology. The categorization of large-scale atmospheric states during SPARTICUS is performed by remapping the occurring weather events onto the 14 year atmospheric state climatology. A short overview and description of some basic meteorological characteristics of the atmospheric states at the ARM SGP site is given in Table 1.

3. Large-Scale Meteorology During SPARTICUS

The climatology of atmospheric states at the ARM SGP site is shown in Figure 1 for the time period 1979–2010. A feature of the distribution of atmospheric states over longer time periods such as multiple years or decades is that the frequency of occurrence of any state is relatively close to the expected value of a uniform distribution (here approximately 4.8% for each atmospheric state). This statistical feature reflects the design of the neural network and is a consequence of the sorting of individual observations within the cluster space (i.e., breaking up large states and deleting smaller ones).

However, on a seasonal time scale, the frequency of occurrence of many states is far away from a uniform distribution and there is clear evidence for variation. In other words, on an interannual time scale, some states occur more frequently than others. In fact, some of the atmospheric states deviating from the uniform distribution the most are convective states typically associated with deep convection over land and occur predominantly during summer and early fall (e.g., states 3, 11, and 15). In contrast, cyclones, frontal systems, or jet streams are more prevalent during winter and early spring when the activity of midlatitude cyclones is highest. About 5 out of 21 states related to deep convection occur most frequently during the summer and fall months (JJA and SON), whereas 11 out of 21 states occur mainly during the winter/spring months (DJF and MAM).

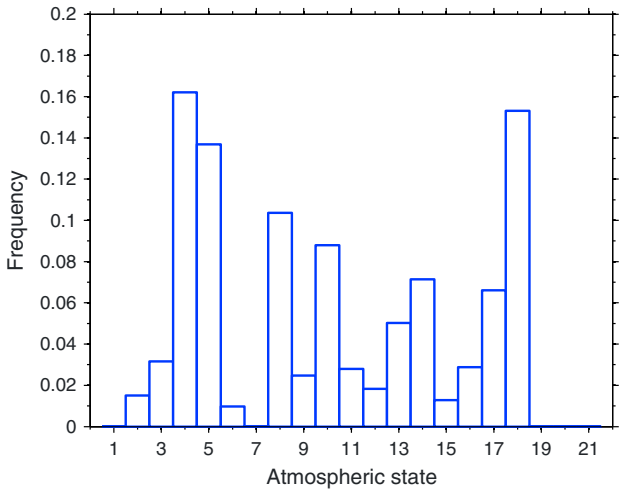

Figure 2. Distribution of the frequency of occurrence of atmospheric states during SPARTICUS research flights. The histogram is normalized such that the sum of all occurrences equals unity.

Figure 2 shows the distribution of atmospheric states that have been sampled by aircraft between January and June 2010 during the SPARTICUS campaign. Although the dynamical and thermodynamical structure of the atmospheric states are different, they all promote the occurrence of cirrus clouds. This underlines the variety of upper tropospheric conditions under which cirrus clouds exist at midlatitudes. The three atmospheric states most frequently sampled during SPARTICUS are upper level ridges (state 4), midlatitude cyclones with embedded cold front (state 18), and subtropical flows with embedded jet streak features (state 5). Almost half of the cirrus cloud occurrences in the vicinity of the ARM SGP site during SPARTICUS can be explained by these three different synoptic conditions. The by far most frequently observed convective state during SPARTICUS is state 10. Examples of the typical synoptic conditions representing each of these states are shown in Figures 3 and 4. Each of these examples represents the nearest centroid member of the cluster; thus, it is the meteorology of the most representative member in the cluster rather than the averaged meteorology of all members. State 4 represents an upper level ridge over North America with the ridge axis centered at the ARM SGP and anticyclonic flows at upper levels. At lower levels, state 4 is characterized by an approaching surface low and southwesterly flows indicating a fair amount of baroclinicity. State 18 represents a deep upper level trough and jet stream to the southeast of the ARM SGP site. At lower levels, state 18 represents a low pressure system centered at the ARM SGP site featuring cyclonic flows and an embedded cold front promoting large gradients in temperature and moisture. State 5 represents an approaching deep trough with embedded jet streak and southwesterly flows at upper levels leading to advection of moist subtropical air toward the ARM SGP site. At lower levels, state 5 features a line of convergence between warm winds from the south and cold winds from the north. The major differences between state 18 and 5 are the vertical wind profile and the moisture flux toward the ARM SGP site. State 18 exhibits strong cyclonic flows at all levels, whereas state 5 features anticyclonically turning winds with height. Also, state 5 has a larger moisture flux at cirrus levels than state 18 for which the influx of moisture is largely at lower levels. The differences in the wind and humidity profiles have implications for the dynamical mechanism by which cirrus forms. During state 18, cirrus is created through the forced ascent of moisture within the frontal system, whereas during state 5, cirrus is created by ageostrophic motions within the jet streak region [e.g., *Mace et al.*, 1995]. The convective state 10 is characterized by relatively weak gradients and low wind speeds at upper levels. At lower levels, state 10 exhibits convergent flows of warm and moist air from the Golf of Mexico at the ARM SGP site. The advection of warm and moist air together with low-level convergence at the ARM SGP site is conducive for buoyancy instability leading to deep convection over Oklahoma.

It is expected and has been well documented that cirrus clouds occur frequently in regions with large-scale uplift such as frontal systems and near jet streams [*Sassen*, 1997; *Spichtinger et al.*, 2005a]. Our finding that cirrus clouds occur frequently in environments with large-scale subsidence such as high pressure systems and upper level ridges is still rather unexpected given what appear to be unfavorable conditions for cloud formation, but it is consistent with results from previous climatological studies of cirrus at midlatitudes [*Mace et al.*, 1997; *Sassen and Campbell*, 2001; *Mace et al.*, 2001]. In fact, during SPARTICUS, about 41% of the observed cirrus occurred in either ridge-type conditions or anticyclonic flows with nearing high pressure systems (state 4 and 8) or after cold fronts (states 2, 6, 13, 17) mainly occurring from January to April 2010. An equal number of cirrus occurrences is observed in troughs with cyclonic activity or warm/cold fronts (states 5, 12, 14, 16, 18) during the same time period. Approximately 18% of observed cirrus cases stem from convective-type conditions (states 3, 9, 10, 11, 15) mainly during April and June 2010.

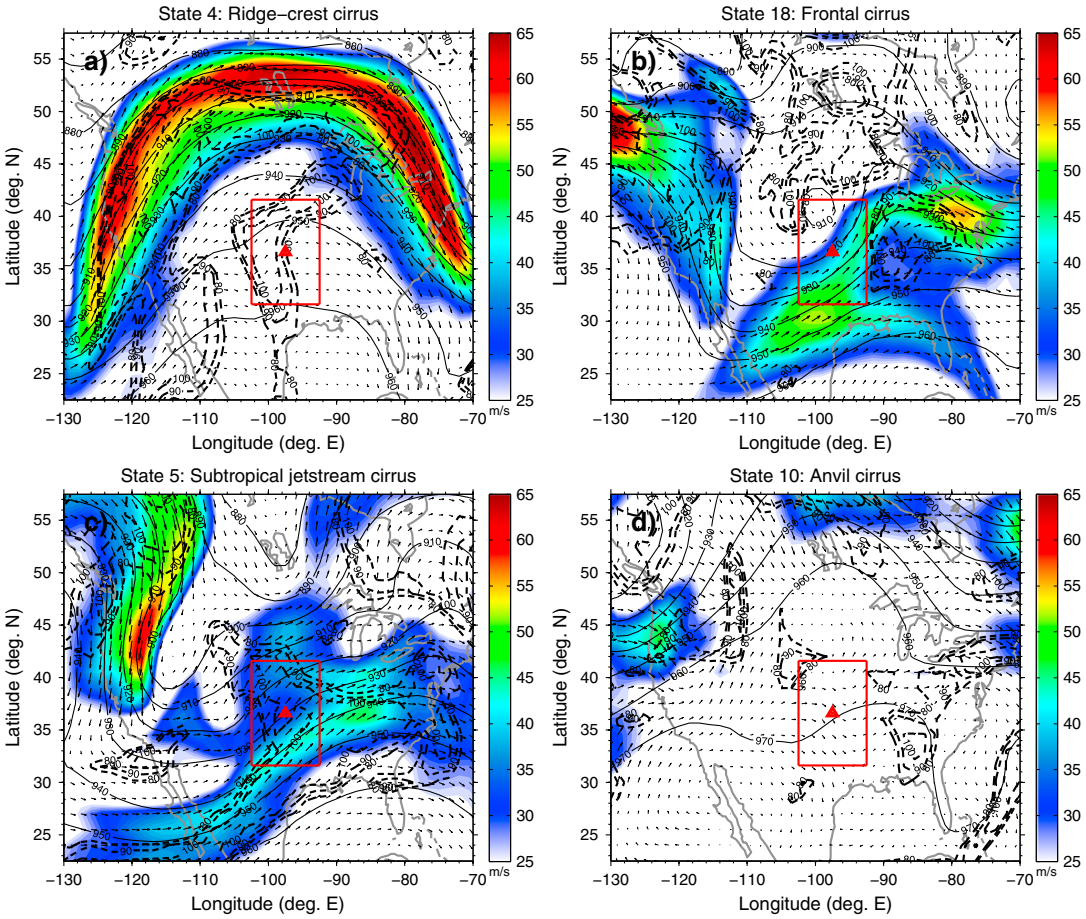

Figure 3. Synoptic conditions of atmospheric states leading to cirrus clouds at the ARM SGP site. Examples are shown for (a) ridge-crest cirrus, (b) frontal cirrus, (c) subtropical jet stream cirrus, and (d) anvil cirrus. Shown are wind speeds (shaded), wind direction (vectors), geopotential heights (solid), and relative humidity with respect to ice (dashed) at the 300 hPa pressure level. Units are m s^{-1} for wind speeds, gpdm for geopotential heights, and percent for relative humidities above 80%. Geographical boundaries are shown in gray, and the location of the ARM SGP site is highlighted with a red triangle. The red box denotes the region used for subsetting and analyzing of the aircraft data throughout this study. These examples are cluster members representing the nearest-to-centroid observation within each cluster rather than mean conditions averaged over all cluster members.

By design, the observational period of SPARTICUS was chosen between January and June for reasons that are twofold. First, winter and spring months are known to exhibit a climatological maximum in the frequency of occurrence of cirrus at the ARM SGP site in Oklahoma [*Mace et al.*, 2006]. Second, the SPARTICUS campaign goal was to sample primarily synoptically driven cirrus and therefore to deemphasize the contributions from convectively generated cirrus during the summer months. Thus, anvil cirrus or cirrus detraining from convective outflows are undersampled in the SPARTICUS data set relative to cirrus generated by synoptic mechanisms other than deep convection. Although none of the synoptic conditions leading to cirrus over the ARM SGP site have been preferred a priori, it cannot be ruled out that SPARTICUS observations are unintentionally biased toward certain meteorological conditions due to the flight planning, decision making, and aircraft operations during the campaign.

Figure 5 shows a comparison between the expected variability in the frequency of occurrence of any given atmospheric state based on the ERA-Interim climatology and the actual frequency of occurrence of the states observed during the SPARTICUS period. From this comparison, we see that there is a higher than normal Rossby wave activity leading to a larger number of upper level ridges (state 4) and troughs/cyclones (state 18) during SPARTICUS. Nevertheless, the number of occurrences of these weather events falls within the expected year-to-year variability and, thus, represents typical conditions at the ARM SGP site during winter and spring. Similarly, there is a higher than normal contribution from subtropical flows (state 5)

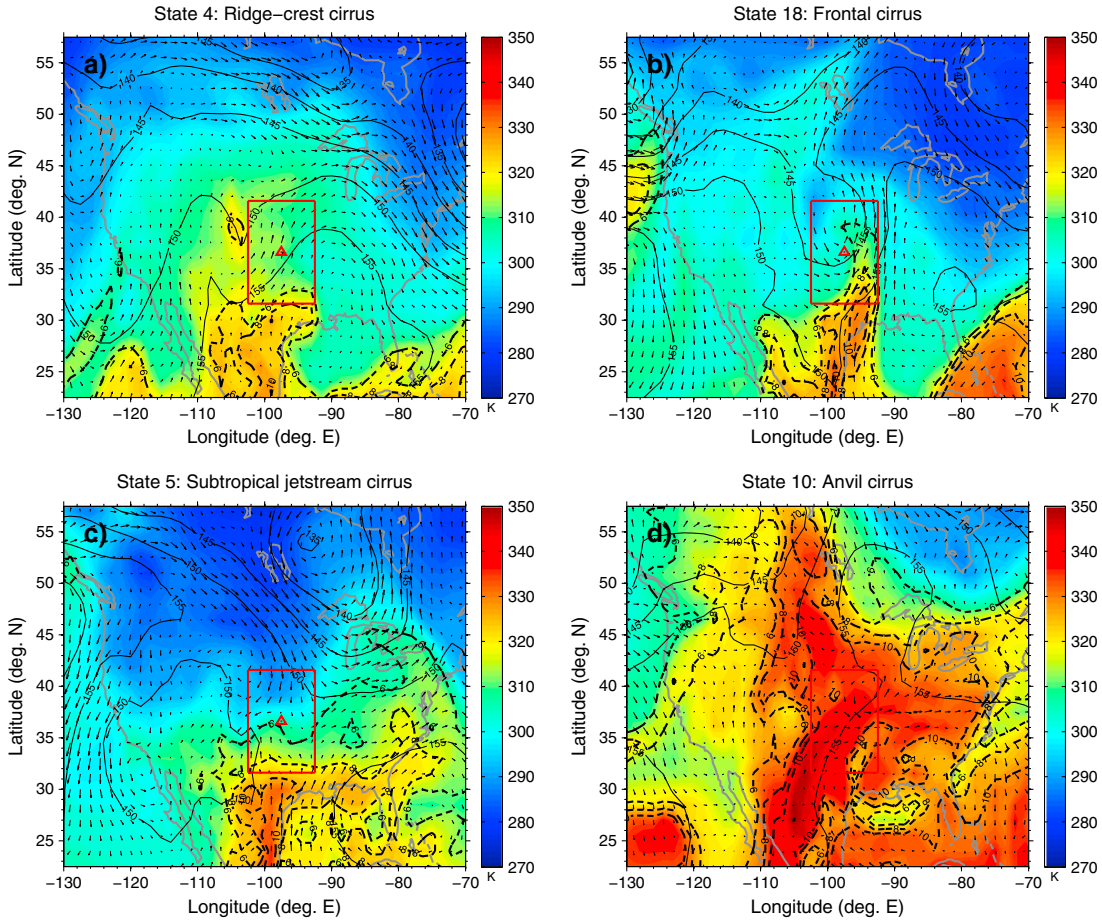

Figure 4. Same as Figure 3 but for potential temperature (shaded), geopotential height (solid), specific humidity (dashed), and wind direction (vectors) at the 850 hPa pressure level.

leading to cirrus cloud occurrence at the ARM SGP site during the SPARTICUS period. In contrast, the contributions from states 6 or 10 exhibit relatively high frequency of occurrences with respect to the climatology. The observations from state 10 indicate an unusually high number of convective events during June not representative of the long-term ARM SGP climatology. For the remainder of the study, we focus on the subset of states featuring cirrus that explain most of the aircraft data set and contain long enough observational records to draw statistically viable conclusions. Thus, we focus on observations from states 4 (upper level ridges; ridge-crest cirrus), 5 (moist subtropical flows; subtropical jet stream cirrus), and state 18 (cyclones with embedded cold front; frontal cirrus). We contrast these typical synoptic cirrus categories with observations representing anvil cirrus and cirrus originating from convective outflow regions typical for state 10.

4. Aircraft Observations

A major objective of SPARTICUS (January–June 2010) is to advance the scientific understanding of microphysical and dynamical processes controlling the evolution and life cycle of midlatitude cirrus by providing a long-term data set of in situ microphysical observations collected by aircraft. In particular, SPARTICUS has been designed to provide further insight into the persistent uncertainties in ice microphysics such as the contributions from small (i. e., < 50 μm maximum diameter) ice crystals to the mass and radiative properties of midlatitude cirrus. This objective is motivated by mounting evidence that our understanding of the occurrence of small ice crystals in cirrus has been biased by in situ aircraft observations frequently showing high ice number concentrations in cirrus. Recent studies suggest that most occurrences of high ice crystal number concentrations are measurement artifacts caused by shattering of ice crystals at the protruding components of cloud probes such as tips, shrouds, and inlets. These shattering effects produce several

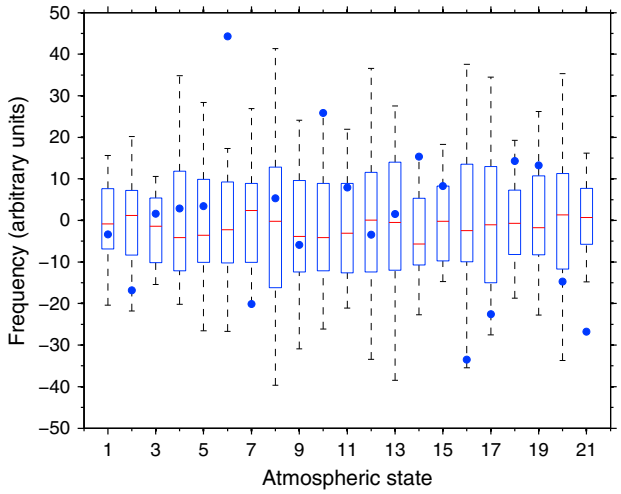

Figure 5. Observed (blue dots) and expected (box and whiskers) variability of the January to June frequency of occurrence of atmospheric states. The frequency of occurrence is plotted in terms of an anomaly with respect to the mean. Data are based on the ECMWF Era-Interim reanalysis for the period 1979–2010. The median is shown as a red horizontal line, boxes indicate the interquartile range (25th to 75th percentile), and the whiskers extend to $\pm 2\sigma$ of the standard normal distribution.

hundreds or even thousands of ice crystal fragments, thereby artificially amplifying the number counts at small particle sizes [*Korolev and Isaac*, 2005; *McFarquhar et al.*, 2007; *Jensen et al.*, 2009; *Korolev et al.*, 2011]. It has been shown that ice shattering artifacts translate into large errors in the measured bulk microphysical properties of cirrus such as ice number concentrations, ice water content, and extinction coefficients [*McFarquhar et al.*, 2007]. Many of the ice microphysical data sets collected with airborne cloud probes during the past 30 years have been widely used, either implicitly or explicitly, in microphysics parameterizations leaving the impact of ice crystal shattering on cloud parameterizations largely unquantified. SPARTICUS addresses the shattering problem by employing new instrument designs and post-processing algorithms that minimize the impact of artifacts on the measurements of ice number concentrations.

4.1. Observational Platform

The primary platform of SPARTICUS is the Stratton Park Engineering Company (SPEC Inc.) Learjet 25. Typical flight patterns flown during SPARTICUS are level legs, ramped ascents/descents, and spirals. During SPARTICUS, the Learjet carried a set of instruments to measure dynamical and thermodynamical quantities such as vertical velocity, temperature, and water vapor, as well as a set of optical cloud probes and particle imagers for measuring particle size distributions (PSDs) and bulk microphysical properties such as ice water content (IWC), ice number concentrations, and crystal habits. Although some of the measurements are collected at sampling rates higher than 1 Hz, all data used throughout this study are reduced to a 1 Hz sampling rate.

4.2. Cloud Probe Data

Measurements of ice crystal number concentrations in midlatitude cirrus with the two-dimensional stereo (2D-S) cloud probe have been obtained recently during the SPARTICUS and NASA Midlatitude Cirrus Properties Experiment (MACPEX) aircraft field campaigns. Throughout this study, we use in situ data from the 2D-S probe to obtain PSDs and bulk estimates of ice number concentrations and IWC in cirrus clouds.

The 2D-S probe has been introduced by *Lawson et al.* [2006] and measures particles in the size range 10–3000 μm with 61 unequally spaced size bins. The smallest 2D-S size bin ranges from 5 to 15 μm (centered at 10 μm) and, thus, captures the small particle end of the PSD to a reasonable degree. The 2D-S is specifically designed to minimize the impact of ice crystal shattering on the sample volume by minimizing protruding instrument surfaces and by using modified probe tips to divert the trajectories of shattering particles from the sample volume. In an effort to minimize the impact of ice particle shattering on the measured PSD, interarrival time algorithms and image processing techniques are used to identify and efficiently remove clusters of small ice crystal fragments resulting from shattering from the 2D-S measurement.

It is possible that a mechanism such as ice crystal clustering could produce an enhancement in nearly coincident interarrival times. *Saw et al.* [2012a, 2012b] provide numerical simulations and laboratory measurements of the inertial clustering of water droplets in homogeneous isotropic turbulence and show that the correlation function increases with decreasing length scale. The correlation function has a smooth, monotonic increase, indicating that the clustering increases smoothly with decreasing length scale, rather than producing a bimodal size distribution which we think is attributable to shattering. Water droplets are weakly inertial with relatively minimal gravitational settling, while ice crystals have a greater inertia and

faster sedimentation rates. In addition, ice particles have a considerably small number density in tropospheric clouds than do water drops. Thus, it likely takes longer times to induce clusters due to turbulence and the clusters are likely to dissipate more quickly due to the larger values of terminal fall speeds. Although we cannot completely rule out ice clustering as the source of the peak in short interarrival times, it seems quite unlikely that it is an important process in producing a local maximum in short interarrival times. Consequently, we attribute the maximum to particle shattering and remove it using the interarrival time technique developed in recent years.

The performance of the 2D-S interarrival time algorithm has been carefully evaluated and is discussed in great detail in *Lawson* [2011]. Details regarding the measurement uncertainties of the 2D-S instrument are discussed in *Lawson et al.* [2006]. The processing of 2D-S image data is a complex process that has evolved based on both theoretical and empirical approaches. The processing can loosely be divided into three broad steps [*Lawson*, 2011]: (1) determination of characteristic lengths and areas of an image, (2) removal of spurious events including electronic noise, optical contamination, particle shattering, and splashing effects, and (3) estimation of bulk physical parameters such as particle number concentration, extinction, and mass as a function of size (these include correction for diffraction effects based on the *Korolev* [2007] methodology and adjustments to sample volume as a function of particle size).

These algorithmic processes require the introduction of various parameters and a set of equations that are defined in *Lawson* [2011, Appendix A and B] and are not reproduced here for the sake of brevity. In recent years, data from the 2D-S with the interarrival time algorithm applied in the same way to remove shattering artifacts have been used in a number of studies on mixed-phase clouds [e.g., *Mitchell et al.*, 2011; *Jackson et al.*, 2012] and ice clouds [e.g., *Jensen et al.*, 2009; *Lawson et al.*, 2010; *Deng et al.*, 2013; *Zhang et al.*, 2013; *Jensen et al.*, 2013].

4.3. Water Vapor Measurements

Measurements of water vapor pressure inside and outside of cirrus clouds are available from the NASA Diode Laser Hygrometer (DLH) instrument. Relative humidity with respect to water and ice is computed from the measured water vapor pressure using the saturation water vapor pressure formulas of *Murphy and Koop* [2005] and the in situ temperature measurements from the Rosemount probe. According to previous analyses of upper tropospheric water vapor measurements by *Kraemer et al.* [2009] and assuming the homogeneous freezing theory of *Koop et al.* [2000] holds, any ice relative humidity data should scatter below the homogeneous freezing threshold of aqueous solution droplets. A hard upper limit in any case should be the water saturation line. Unfortunately, some of the SPARTICUS water vapor measurements are affected by an internal humidity problem with the DLH, thus leading to unrealistically high and partly unphysical measurements of ice relative humidity. About 7% of the DLH RHI data are above water saturation and another 3% are below water saturation but above the homogeneous freezing threshold. Only measurements below the water saturation line and below the threshold humidity for homogeneous freezing are used for analysis throughout this study. None of the other measurements used in this study are affected by this problem.

4.4. Vertical Velocity Measurements

Vertical velocities are obtained from the AIMMS-20 instrument carried by the aircraft. Unfortunately, absolute measurements of vertical velocity are uncertain due to the poor absolute accuracy of the instrument. According to the AIMMS-20 manual, the absolute accuracy of the vertical velocity measurements from the AIMMS-20 is approximately ± 0.75 m s^{-1}, which is typically on the same order of magnitude as observed vertical velocities in the upper troposphere [*Gultepe et al.*, 1990]. However, *Lenschow* [1972] argues that the random component of errors in measured vertical air motions is considerably lower than the bias component. Thus, similar to previous studies, we derive the perturbation vertical velocities by subtracting the mean vertical velocity and best estimate linear trend along constant-altitude flight legs.

An automated technique is used for identifying constant-altitude flight legs and is based on two statistical tests applied to the aircraft height measurements and aircraft vertical motions along each 30 s flight segment. Since on a level leg the distribution of aircraft vertical velocities follows a normal distribution with zero mean but unknown standard deviation, the null hypothesis (i.e., the mean of the aircraft vertical velocity distribution is not different from 0) can be tested with a simple *t* test. If the null hypothesis is true, the flight segment is identified as level leg and vice versa. The second statistical test involves estimation of the mean ascent/descent rate of the aircraft during each flight segment from the slope parameter of a simple linear least-squares regression model fitted to the sequence of aircraft height measurements. If the total

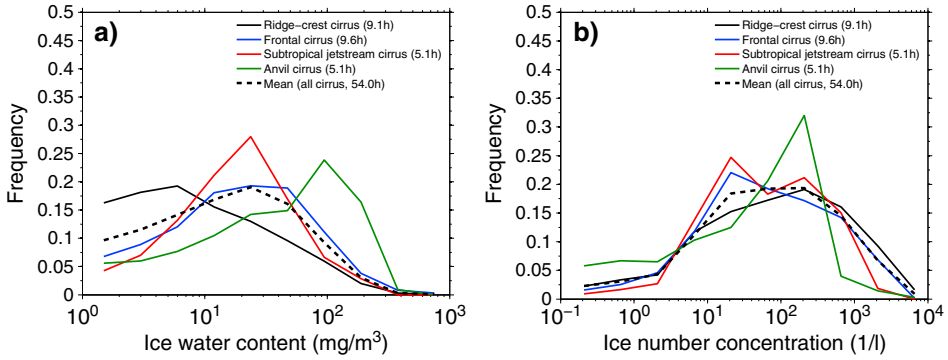

Figure 6. Probability density functions of (a) ice water content and (b) ice number concentration composited by atmospheric state. The numbers in brackets indicate the number of research flight hours going into each curve.

height deviation along a 30 s flight segment is less than 15 m (corresponding to a height slope of less than 0.25%), the flight segment is classified as level leg. Based on visual inspection, combining both tests gives excellent results for the identification of level flight legs.

5. Analysis

During SPARTICUS, approximately 200 h of flight time were spent on the collection of in situ aircraft data. However, in order to exclude possible mixed-phase conditions, only aircraft data collected below a typical temperature threshold of −30°C for cirrus clouds is considered throughout this study. Thus, the subset of the aircraft data set used in this study is representative of midlatitude cirrus with cloud bases above approximately 7 km altitude. Since some of the research flights during SPARTICUS were conducted away from the ARM SGP site, we limit our analysis to data inside a $10 \times 10°$ area centered at the ARM SGP site for which similar meteorological conditions are guaranteed based on the atmospheric state classification. These constraints reduce the amount of in situ aircraft data used in the subsequent analysis to about 50 h. Changing the size of the limited domain does affect the sample sizes in the statistical analysis but does not qualitatively change the results. Similarly, changes in the temperature threshold by ±5 °C have little impact on the overall statistics.

5.1. Bulk Microphysical Properties

Figure 6 shows probability density functions (PDFs) of in situ aircraft measurements composited by atmospheric state for the states that contribute most to cirrus cloud occurrence during SPARTICUS (i.e., upper level ridges, cyclones with embedded cold front, and subtropical flows). The statistics of cirrus ice water content and ice number concentrations exhibit striking differences among the different synoptic regimes. The statistics of cirrus microphysical properties (i.e., the cumulative density functions and the mean of the distribution) are tested with two nonparametric tests, namely, a two-sample Kolmogorov-Smirnov test and a two-sided Wilcoxon rank sum test, and both tests suggest that the differences among the PDFs are statistically significant at the 95% confidence level. The number of research flights and days of observations considered in the statistics are listed in Table 2.

Cirrus clouds sampled during upper level ridges show lower ice water content than cirrus clouds forming in subtropical flows or cirrus triggered by deep convection over land. Although, ridge-type cirrus are forming in environments with considerable ice supersaturation, the ice water content is generally lower due to the

Table 2. Number of Research Flights, Number of Days, and List of Days for Which SPARTICUS Observations are Taken Into Account for the Various Considered Cirrus Categories and Atmospheric States[a]

State Number	Cirrus Category	Number of Research Flights	Number and List of Days
4	Ridge-crest cirrus	10	5 (Mar 19, 30, Apr 01, 28, 29)
5	Subtropical jet stream cirrus	9	7 (Jan 14, 15, 31, Feb 01, 03, 04, 11)
10	Anvil cirrus	6	5 (Jun 11, 14, 15, 17, 18)
18	Frontal cirrus	10	7 (Jan 19, 20, 21, Mar 10, 11, 27, Apr 24)

[a]All observations are from year 2010.

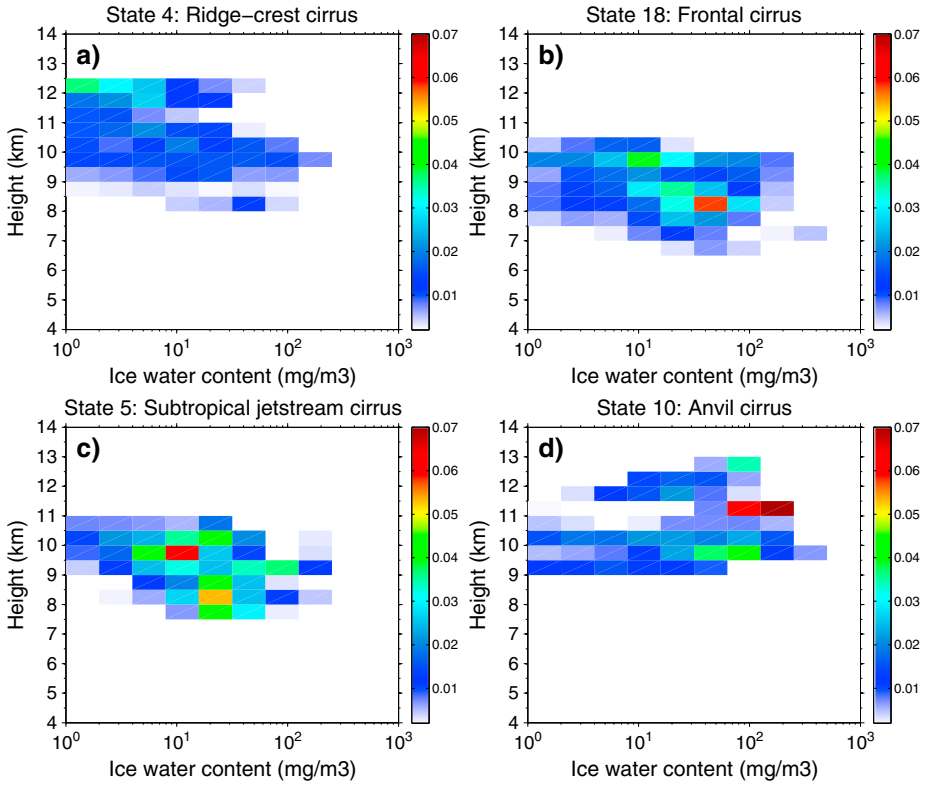

Figure 7. Joint histograms of ice water content as a function of height composited by atmospheric state for (a) ridge-crest cirrus, (b) frontal cirrus, (c) subtropical jet stream cirrus, and (d) anvil cirrus.

lack of water vapor available under these conditions. In contrast, all other categories benefit from a substantial influx of water vapor though the meteorological reasons for the water vapor flux are different in each cirrus category as discussed in section 3.

Ice number concentrations are highest in cirrus clouds forming in upper level ridges and lowest in the anvil/convective outflow cirrus categories sampled during SPARTICUS. The low particle number concentrations in the latter seem counterintuitive but are explained by the fact that during SPARTICUS anvil cirrus and cirrus detrained from convective outflow regions are microphysically aged as they are sampled far away from the convective cores. Previous studies show that both ice water content and ice number concentrations decrease rapidly in aging anvil cirrus drifting away from convective sources but also point out that ice particle number concentrations exceeding 10 cm^{-3} can be found in fresh anvils near convective towers [*Lawson et al.*, 1998, 2010].

The frequency of occurrence of cirrus ice water content is shown as a function of height and temperature in Figures 7 and 8, respectively. The ice water content is generally found to increase with decreasing height but increasing temperature as low ice water contents typically occur at cloud tops and increase toward cloud base as a result of ice particle growth by deposition and aggregation. The frequency of occurrence for high ice water contents is largest for the anvil/convective outflow cirrus category, followed by cirrus forming in subtropical flows and frontal systems and lowest for the ridge-crest cirrus category. Also the cloud tops of ridge-crest cirrus are found at higher altitudes and lower temperatures than the other synoptically driven cirrus categories except anvil cirrus. Although the cloud tops of the anvil cirrus category are at similar heights, they occur at considerably warmer temperatures.

The frequency of occurrence of ice number concentrations is shown as a function of height and temperature in Figures 9 and 10, respectively. For most cirrus categories, the highest ice number concentrations are typically found at higher altitudes and lower temperatures, which is consistent with the idea of ice nucleation occurring primarily at the cold cirrus cloud tops. High frequency of occurrence of high ice number concentrations is typically found well below the homogeneous freezing temperature of pure liquid water at around −40°*C*. However, there is also indication of high occurrences of lower ice particle number

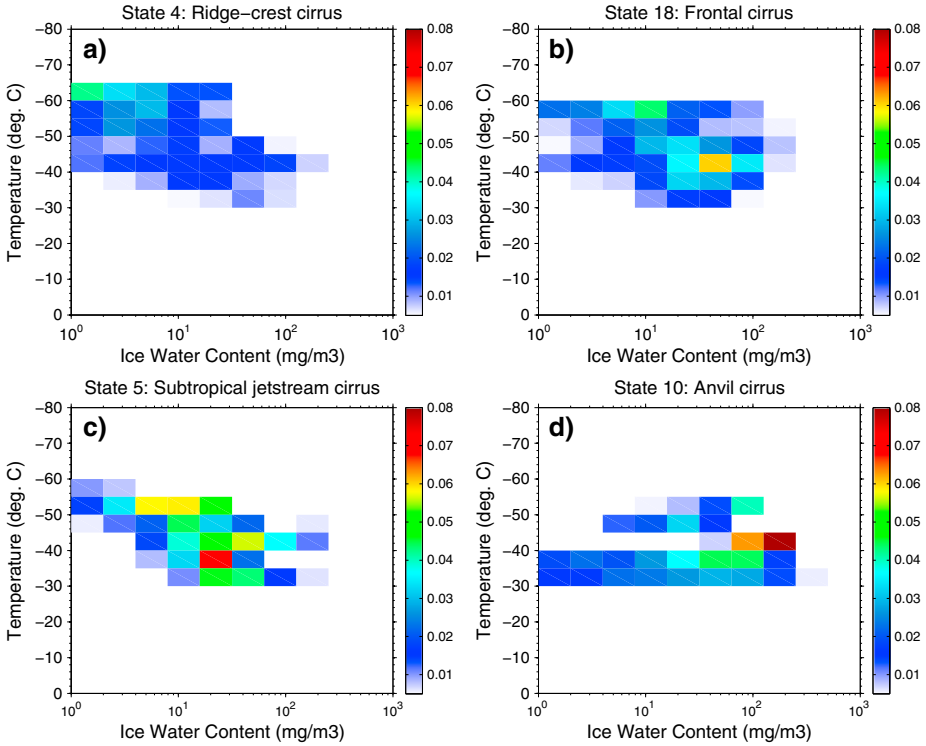

Figure 8. Same as Figure 7 but as a function of temperature.

concentrations at temperatures considerably warmer than −40°*C* in cirrus generated by moist subtropical flows, which may be indicative of significant contributions of ice crystals freezing heterogeneously. However, an alternative explanation could be the growth of ice particles by aggregation followed by sedimentation, thereby lowering the cirrus particle number concentrations. The highest occurrence of small ice crystals (i.e., high ice number concentrations and low ice water content) is found in the ridge-type conditions and is consistent with high (up to 12 km) and cold (down to −65°C) cloud tops that are sampled in this particular cirrus category. In contrast, cirrus cloud tops in the frontal category do typically occur at lower altitudes of approximately 10 km and warmer temperatures down to about −60°C (Figures 7–10).

5.2. Particle Size Distributions

Particle size distributions (PSDs) are investigated by aggregating and averaging the measured 1 Hz particle spectra over 5 s intervals. Given an aircraft true airspeed of approximately 200 m s^{-1}, temporal averaging of 5 s correspond to a spatial averaging of approximately 1 km distance along the aircraft flight path as in *Heymsfield* [2003a, 2003b]. Similar to previous studies, we fit the observed particle spectra with gamma distributions of the form

$$F(D) = N_0 D^{\nu} \exp(-\lambda D) \tag{1}$$

to obtain the size distribution parameters, which are the intercept parameter N_0, the shape parameter ν, and the slope parameter λ. D is the maximum diameter of the particle. Gamma distributions have been widely used to fit observed PSD in cirrus and, by allowing for a variable shape parameter, are found to represent the variability in the observed PSDs to a better degree than exponential distributions [*Mitchell*, 1991; *Ivanova et al.*, 2001; *Heymsfield*, 2003b].

The procedure to fit the observed particle size spectra is based on work by *Kozu and Nakamura* [1991] and *Heymsfield et al.* [2002] and is briefly reviewed. The PSD parameters are estimated by simultaneously matching three moments of the observed size distribution. Following *Heymsfield et al.* [2002], we use the first (diameter), second (area), and sixth (reflectivity) moments of the measured PSD in the fitting procedure. The pth complete moment of the gamma distribution is given by

$$M_p = \int_0^{\infty} D^p F(D) \mathrm{d}D = \frac{N_0 \Gamma(\nu + p + 1)}{\lambda^{\nu+p+1}} \tag{2}$$

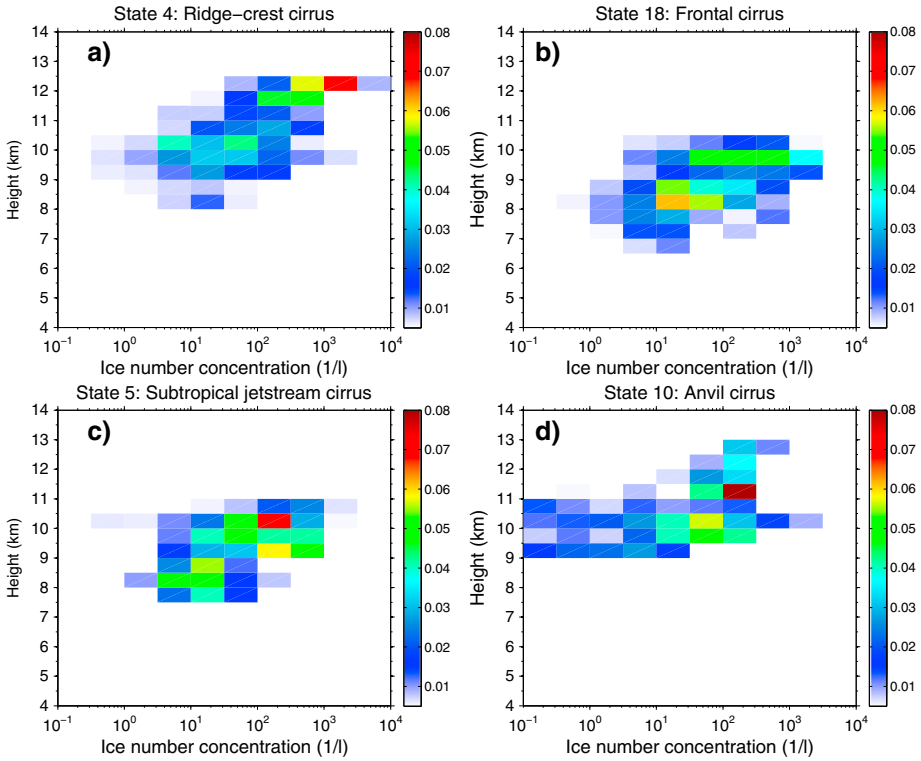

Figure 9. Joint histograms of ice number concentration as a function of height composited by atmospheric state for (a) ridge-crest cirrus, (b) frontal cirrus, (c) subtropical jet stream cirrus, and (d) anvil cirrus.

with the gamma function $\Gamma(x) = \int_0^\infty t^{x-1} \exp(-t)\mathrm{d}t$ for $x > 0$ and $\Gamma(x+1) = x\Gamma(x)$. Using the first moment M_1 and the second moment M_2 in the expression for the sixth moment M_6, defining $F = M_2^5 / \left(M_1^4 M_6\right)$ and solving for the shape parameter ν give the following fourth order polynomial equation:

$$(1-F)\,\nu^4 + (8-18F)\,\nu^3 + (24-119F)\,\nu^2 + (32-342F)\,\nu + 16 - 360F = 0 \tag{3}$$

Thus, the shape parameter ν can be derived by finding the real roots of the polynomial equation (3) subject to the boundary condition $\nu > -1$. The intercept parameter N_0 and slope parameter λ are then given by

$$N_0 = \frac{M_1 \lambda^{\nu+2}}{\Gamma(\nu+2)} \tag{4}$$

and

$$\lambda = \frac{M_1\,(\nu+2)}{M_2}, \tag{5}$$

respectively. Because previous studies found that PSDs in cirrus can exhibit considerable bimodality [e.g., *Ivanova et al.*, 2001; *Zhao et al.*, 2011], we separate the particle size spectrum into small- and large-particle modes and fit gamma distributions to each of the particles modes. The fixed threshold particle size separating the small-particle mode from the large-particle mode is chosen to be D_s =100 μm based on visual inspection of the PSDs and is similar to *Ivanova et al.* [2001]. To ensure that the PSD fits have reasonable quality, we apply a simple data acceptance criterion that filters out all time averaged PSD segments that do not contain data in at least 30 % of the size bins. Furthermore, only fits for which the coefficient of determination R^2 is larger than 0.6 are considered.

Figure 11 shows the mean PSD for each cirrus category. Although there is no compelling evidence of distinct bimodal features in the averaged PSDs in terms of two distinct peaks, there is indication of two populations of particles sizes if PSDs are composited by atmospheric state or temperature. The two particle populations manifest themselves in terms of a narrower small-particle mode with elevated number concentrations of

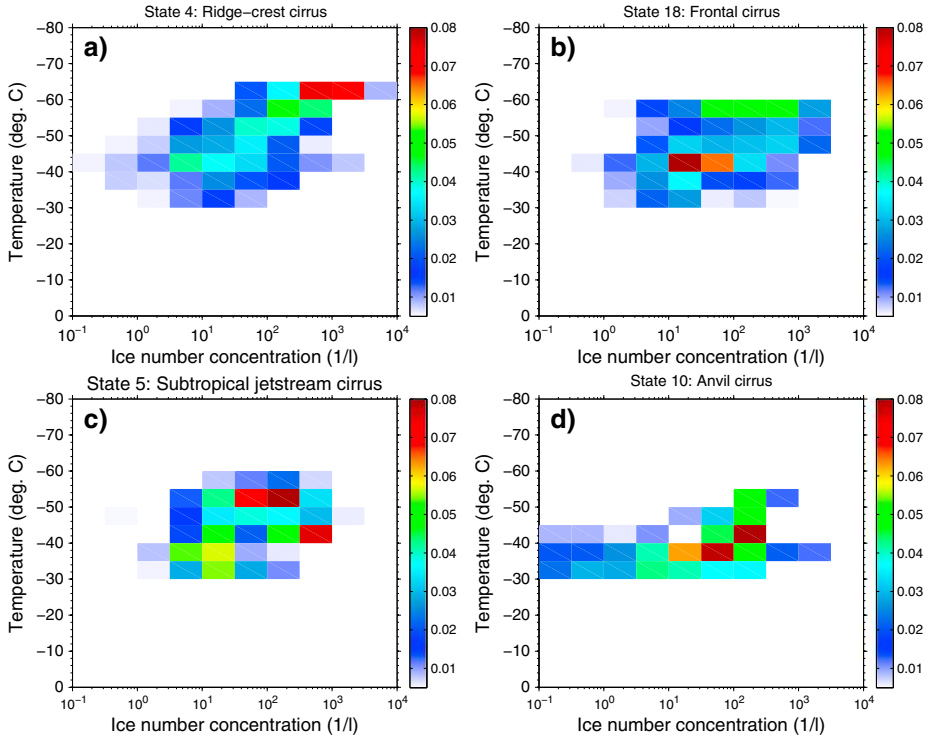

Figure 10. Same as Figure 9 but as a function of temperature.

particles at smaller sizes and a broader large-particle mode separated from each other by a plateau at diameters somewhere between approximately 40 and 100 μm. The bimodal features are more evident in the case of subtropical and anvil cirrus, whereas PSDs in ridge-crest and frontal cirrus conditions exhibit monomodal size distributions.

A similar separation of the data is seen if the PSDs are first composited by temperature and then averaged. PSDs in cold cirrus (T ≤ 235K) such as under ridge-crest type conditions tend to be monomodal, whereas PSDs in warmer cirrus (T > 235K) exhibit a plateau at size ranges between approximately 70 and 200 μm. Unfortunately, the 2D-S probe does not have sufficient resolution to detect particles below about 5 μm in size, and thus, we do not see a decline in particle number concentrations at sizes below 10 μm as, for example, in the data presented by *Ivanova et al.* [2001]. However, a decline in the number concentrations at small sizes is seen in measurements taken by the Fast Forward Scattering Spectrometer Probe (F-FSSP), which has higher resolution than the 2D-S at small sizes. Whether the elevated number concentrations at small sizes are physically founded or an artifact of measurement uncertainty is debatable needs further

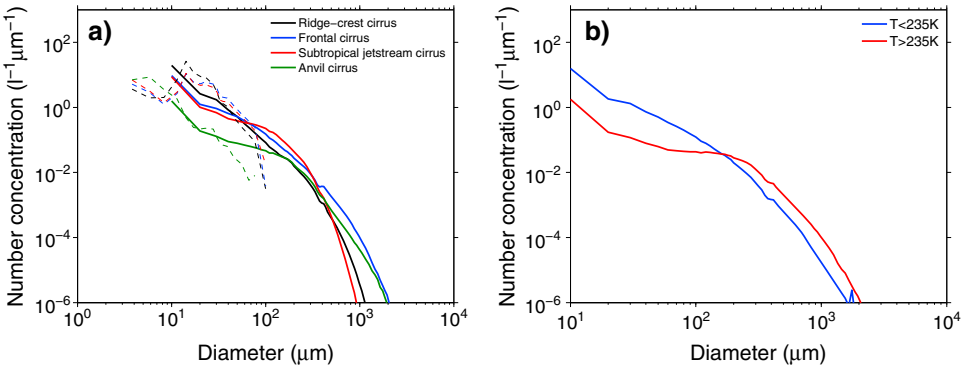

Figure 11. Mean particle size distributions composited by (a) atmospheric state and (b) temperature. Solid lines are based on data from the 2D-S probe, whereas dashed lines are based on data from the F-FSSP.

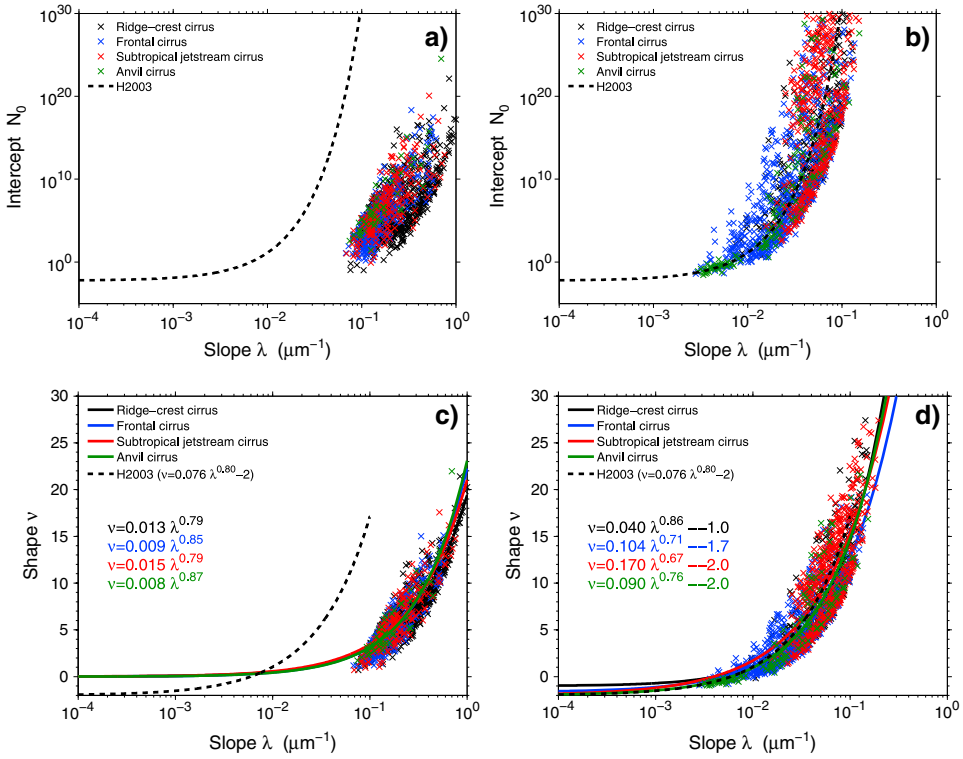

Figure 12. Statistical relationships of the fitted PSD parameters as a function of the slope parameter λ for (a, c) the small-particle mode and (b, d) the large-particle mode. The data are subsampled for plotting purposes, and only one out of four data points is plotted to decrease the clutter. Power law fits based on all data are shown together with relationships found previously by *Heymsfield* [2003b].

investigation. PSDs of all cirrus categories except the ridge-crest cirrus exhibit a broader shoulder indicative of a large-particle mode.

There is clear evidence for higher number concentration of small particles with sizes smaller than about 60 μm in the ridge-crest cirrus category. Particle number concentrations at the small bin sizes are at least a factor of 2 higher in the ridge-crest cirrus category than in any other cirrus category, which suggests that particle generation by nucleation is more active and important in cirrus forming under ridge-type conditions. This result is consistent with our previous finding that cirrus in the ridge-crest category form at high altitudes with cold cirrus cloud top temperatures down to about −60°C.

The lack of a large-particle mode and the narrower averaged size spectrum of cirrus in the ridge-crest category is suggestive of an inefficient particle growth regime despite the relatively high ice supersaturations found under these conditions (see analysis of relative humidity data later). Possible explanations for the inefficient growth of ice crystals are the lack of water vapor to grow particles to larger sizes through diffusional growth or longer water vapor relaxation times due to kinetic limitations of ice particle growth at low temperatures. In contrast, all other cirrus categories promote wider particle size spectra and show considerable higher number concentrations of particles at larger (i.e., D ≥500 μm) sizes, which is indicative of a more prominent role of depositional growth and aggregation under these conditions.

Figure 12 shows the fitted size distribution parameters and the slope parameter λ for the various cirrus categories. Similar to *Heymsfield et al.* [2002] and *Heymsfield* [2003b], we find well-defined statistical relationships among the size distribution parameters for cirrus forming under various conditions. For example, both the intercept parameter N_0 and the shape parameter ν increase with increasing slope parameter λ. For the large-particle mode, the relationship between intercept and slope as well as between the shape and slope found from the SPARTICUS 2D-S data obeys power laws and is qualitatively similar to the relationships obtained by *Heymsfield* [2003b] for midlatitude cirrus. However, there is considerable variability depending on the cirrus category and significant differences in the estimated fit coefficients since the 95% confidence intervals of the fitted curves do not overlap. The estimated exponents of the ν-λ relationships range from

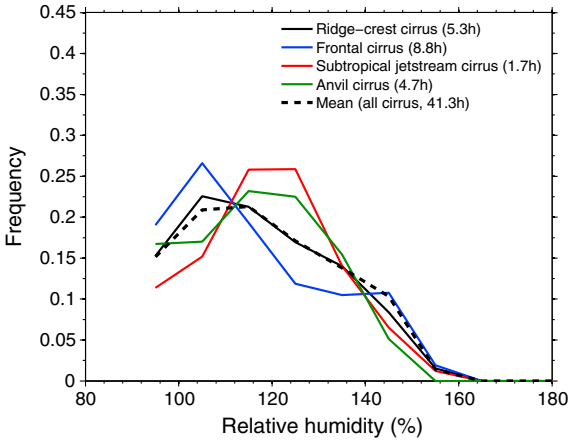

Figure 13. Same as Figure 6 but for ice relative humidity.

0.67 to 0.87 depending on particle size range and atmospheric state but include the value of 0.8 found by *Heymsfield* [2003b]. Especially for the small-particle mode, the previously obtained relationships do not hold, and in fact for the same intercept and shape parameter, the slope parameter is about an order of magnitude higher. Potential explanations for the disagreement with the results of *Heymsfield* [2003b] are twofold: First, *Heymsfield* [2003b] omitted bimodal PSDs and second, PSDs are obtained from a 2-DC probe with a detection limit of 50 μm, which is somewhat larger than the 2D-S probe used throughout this study.

Ridge-crest cirrus indicate higher frequency of occurrence for size distributions with larger shape and slope parameter indicative of narrower size distributions and lower ice fall speeds and sedimentation rates (not shown). The latter is consistent with findings by *Heymsfield* [2003b] showing generally an inverse relationship between the slope parameter λ and temperature and the largest values of λ occurring at the lowest temperatures.

5.3. Relative Humidity

Consistent with the PDFs of ice number concentrations in the different cirrus categories, the PDFs of relative humidity with respect to ice (Figure 13) exhibit long tails and generally higher probabilities of high ice supersaturations (i.e., larger than 140%) in the ridge-type cirrus category. Lowest ice supersaturations are observed in the anvil cirrus category, which is consistent with the relatively low ice number concentrations but high values of IWC observed in these cases. Mean in-cloud supersaturations are approximately 17% above ice saturation, which is somewhat higher than the 13% above ice saturation reported by *Gao et al.* [2004] during CRYSTAL FACE.

5.4. Vertical Velocities

Vertical velocities measured with an AIMMS-20 instrument are analyzed along constant-altitude flight legs.

Figure 14 shows the PDFs of perturbation vertical velocity composited by atmospheric states for all data collected inside and outside of cirrus. Typical vertical velocities at midlatitude cirrus altitudes are on the order of $\pm$ 1 m s^{-1}. The PDFs of perturbation vertical velocities obey normal distributions with a mean close to 0 and a standard deviation of about $\sigma_w = \pm 0.43$ m s^{-1}. Overall, there is little difference between the PDFs of vertical velocities inside versus outside of cirrus but the variability of vertical velocities inside cirrus ($\sigma_w = \pm 0.46$ m s^{-1}) is somewhat higher than the variability outside of cirrus clouds ($\sigma_w = \pm$ 0.41 m s^{-1}). However, the variability of perturbation vertical velocity inside cirrus determined from the aircraft data set is considerably higher than the variability of $\sigma_w = \pm 0.27$ m s^{-1} reported by [*Kalesse and Kollias*, 2013] from multiple years of Doppler radar data at the ARM SGP site. Possible explanations for the discrepancy may be differences in the sampling period (multiple month versus multiple years) or differences caused by the measurement or analysis technique. Interestingly, there is virtually no difference in the perturbation vertical velocities in the various dynamical regimes and the PDFs are statistically not different. This result suggests that although there may be lagged correlations between vertical velocities and

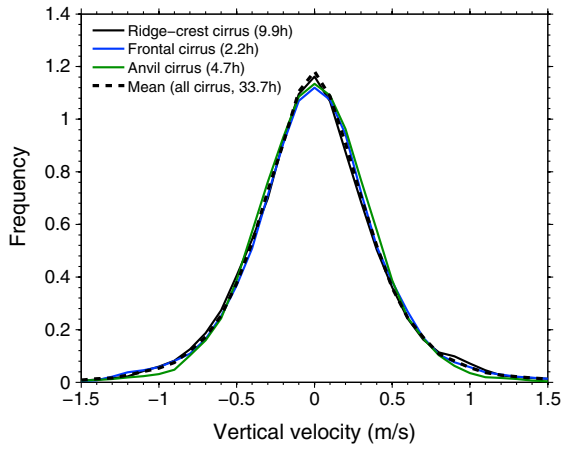

Figure 14. Same as Figure 6 but for perturbation vertical velocity.

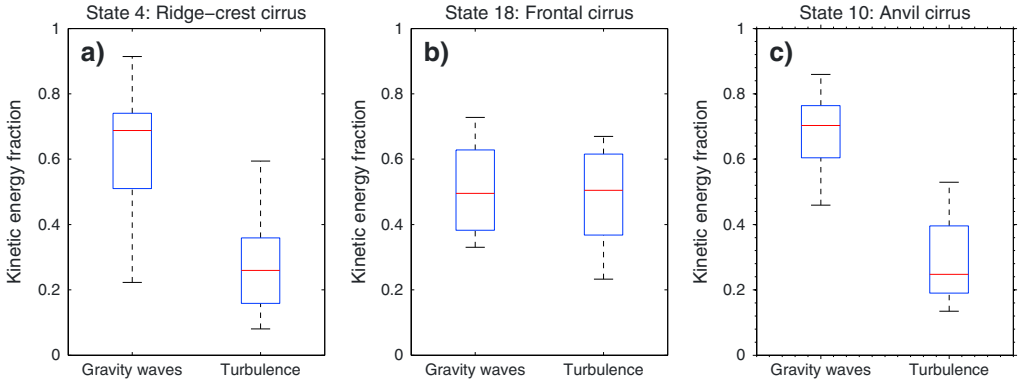

Figure 15. Box-whisker plots of the fraction of kinetic energy contained in wavelengths bands representative of gravity waves and turbulence/embedded convection composited by atmospheric state for (a) ridge-crest cirrus, (b) frontal cirrus, and (c) anvil cirrus.

cirrus microphysical properties (e.g., ice number concentrations) in certain cases, the PDFs of vertical velocity sampled over many cases are a poor predictor of the microphysical properties of cirrus clouds and cannot be used to constrain the cirrus microphysical variability. In order to further investigate the role of vertical velocity perturbations among the different atmospheric states, a spectral analysis is performed.

The spectral analysis of the perturbation velocity data is performed to identify the role of turbulence and wave activity and to calculate energy spectral densities and spectral slopes of the inertial subrange. Further, we obtain estimates for the contributions of turbulence and waves to the observed vertical velocity perturbations. In previous studies, various techniques have been applied to vertical velocity measurements to obtain spectral information such as wavelet analysis [e.g., *Kalesse and Kollias*, 2013], structure function methods, and fast Fourier transform (FFT) analysis [e.g., *Gultepe and Starr*, 1995]. The latter method is also applied in this study to compute the kinetic energy spectral density $E(\kappa)$ for wave number $\kappa = 2\pi f/U_a$, frequency f, and horizontal aircraft velocity U_a. The wavelength is calculated from the true aircraft speed and frequency as $\lambda = U_a/f$. Kinetic energy fraction is defined here as the fraction of kinetic energy $\int_{\kappa}^{\kappa+\Delta\kappa} E(k)\mathrm{d}k$ contained in a defined wave number interval $[\kappa, \kappa + \Delta\kappa]$ to the total kinetic energy $\int_0^{\infty} E(k)\mathrm{d}k$. The fractional kinetic energy is computed for two wavelength bands, namely, gravity waves with wavelengths $\lambda > 5$ km and turbulent motion with $\lambda \leq 5$ km. The spectral slope in the inertial subrange is determined from a linear regression of $\ln(\kappa)$ against $\ln E(\kappa)$ for all wavelength $\lambda \leq 5$ km. The choice and definition of wavelengths bands is mainly motivated by previous studies but is also due to limitations of the aircraft data to identify wave motions on larger scales as a result of the relatively short horizontal flight legs. Most of the SPARTICUS flight legs are between 2 and 5 min, which limits the maximum detectable wavelengths to less than about 70 km and, thus, the gravity wave spectrum. However, a few legs with lengths up to 10 min also allow the detection of modes from large gravity waves or mesoscale waves ($\lambda \approx 100$ km). *Kalesse and Kollias* [2013] find gravity wave activity over the ARM SGP site with typical wavelengths of about 10 km during summer and between 20 km and 70 km during winter. The longer gravity wave modes are associated with synoptic-scale weather perturbations, whereas the shorter wavelengths are related to convective activity. *Quante* [2006] report a wavelength range of about 2–5 km as the threshold between turbulence and waves. Our turbulence category includes small-scale overturning motions resulting from embedded convection within unstable or neutrally stratified layers in cirrus. A true aircraft speed of about 200 m s^{-1} on average results in a Nyquist frequency of 0.5 Hz that limits the lowest detectable wavelength in the aircraft data to about 400 m.

Figure 15 shows the fraction of kinetic energy contributed from the two different wavelength bands. For most cirrus in the ridge-crest category (state 4) and anvil category (state 10), about 70% of the kinetic energy originates from gravity and mesoscale wave modes with considerably smaller contributions turbulence at smaller scales. In contrast, for cirrus forming in frontal systems (state 18), contributions from gravity/mesoscale waves and turbulence/embedded convection are the same order of magnitude. Contributions from mesoscale waves can be appreciable, but in the majority of the cases, the energy fraction from mesoscale waves is less than about 10%. Unfortunately, no data exist for the subtropical jet stream cirrus category (state 5) due to instrument malfunction during these flights.

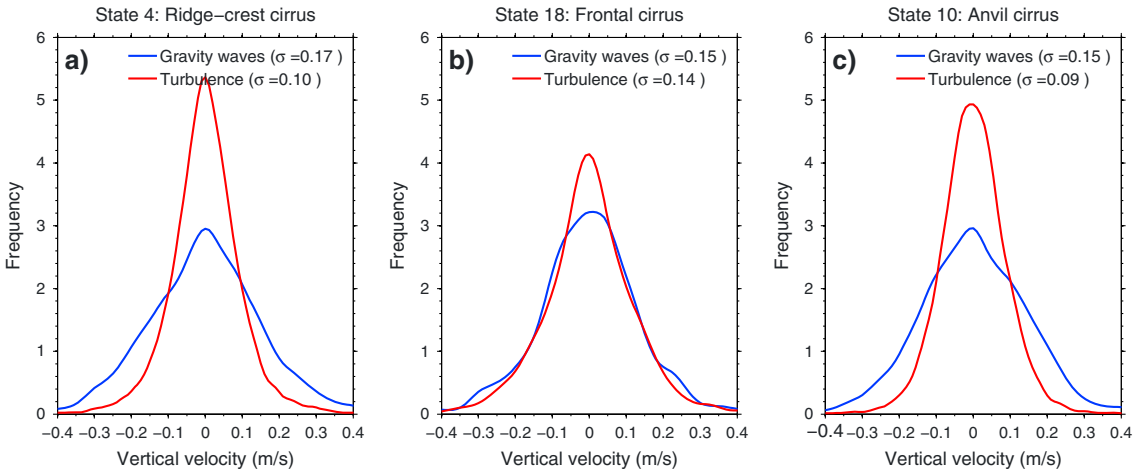

Figure 16. PDFs of vertical velocity contributions from gravity waves (blue) and turbulence/embedded convection (red) composited by atmospheric state for (a) ridge-crest cirrus, (b) frontal cirrus, and (c) anvil cirrus.

Figure 16 shows PDFs of contributions to the vertical velocity from gravity/mesoscale waves and turbulence/embedded convection, respectively. Vertical velocity contributions from gravity waves are on the order of ± 0.4 m s^{-1} with little variability among atmospheric states. However, the variability of contributions from turbulence/embedded convection is significantly larger. The contributions from gravity/mesoscale waves and turbulence/embedded convection to the vertical velocity are about equal for ridge-type conditions (state 4) and anvil cirrus (state 10). In contrast, for cirrus forming in frontal systems, the vertical velocity contributions from turbulence/embedded convection outweighs the contributions from wave activities. Contributions from mesoscale waves are typically on the order of 10 cm s^{-1}, which is in rough agreement with estimates from previous aircraft campaigns such as FIRE I and FIRE II [*Gultepe et al.*, 1995; *Gultepe and Starr*, 1995], but considerable uncertainty is attached to this estimate due to the limited number of long flight legs.

An analysis of the spectral slope of the inertial subrange (here defined as all wavelength smaller than 5 km) shows that for the majority of the cases spectral slope estimates range from −1.6 to −2.5 similar to recent estimates inferred from Doppler radar by *Kalesse and Kollias* [2013]. On average, the estimates of the spectral slope are relatively close to the theoretical $\kappa^{-5/3}$ dependence for the ridge-crest cirrus and frontal cirrus categories (state 4 and 18) and indicative of isotropic three-dimensional turbulence. However, there is considerable variability especially toward steeper slopes. For example, some cases suggest a spectral dependence between κ^{-2} and $\kappa^{-2.4}$ associated with weakly interacting gravity waves or intermittent turbulence. The occurrence of intermittent turbulence in clouds can be attributed to strong wave interactions or intermittent convective activity [*Gultepe and Starr*, 1995], which is consistent with the anvil cirrus category.

6. Conclusions

In this study, we use an objective atmospheric state classification for the ARM SGP site as a statistical tool to identify and categorize synoptic-scale weather events during the SPARTICUS campaign and as a basis for compositing in situ microphysial observations of cirrus by large-scale meteorology. The approach allows for drawing statistically viable conclusions of the statistical relationships between cirrus microphysics and the large-scale dynamical and thermodynamical properties of the atmosphere. The atmospheric state classification is informed about the large-scale meteorology and state of cloudiness at the ARM SGP site by using ECMWF ERA-Interim reanalysis and 14 years of continuous observations from the MMCR.

Almost half of the cirrus cloud occurrences in the vicinity of the ARM SGP site during SPARTICUS can be explained by three distinct synoptic conditions, namely, upper level ridges, midlatitude cyclones, and associated cold fronts and subtropical flows with embedded jet streak features. Probability density functions (PDFs) of bulk microphysical properties (in particular PSDs, ice number concentrations, IWC) exhibit striking differences among the different synoptic regimes with low ice water contents but high ice number concentrations found near the cloud tops of cirrus forming under ridge-type conditions. In contrast, cirrus

sampled during subtropical flows and aged anvils blown off deep convective towers show considerably lower ice number concentrations but higher ice water contents. During SPARTICUS, small particles are most frequently found at low temperatures and high altitudes within upper level ridges. The presence of gravity wave modes together with patches of high ice supersaturation at upper levels promotes the formation and maintenance of cirrus within upper level ridges despite indications of large-scale subsidence.

PSDs of cirrus exhibit narrow size spectra indicative of inefficient particle growth in the ridge-crest cirrus category, despite the occurrence of high relative humidities, whereas all other cirrus categories promote wider PSDs with considerable higher number concentrations of larger particles due to depositional growth and aggregation. Possible explanations for the inefficient particle growth regime may be kinetic limitations such as low water vapor deposition coefficients at lower temperatures or the lack of sufficient water vapor to promote particle growth to sizes large enough for aggregation to take place.

Similar to previous studies, we find well-defined statistical relationships among the size distribution parameters for cirrus forming under various environmental conditions. For the large-particle mode, the relationships between intercept and slope parameter as well as between shape and slope obey power laws and are qualitatively similar to previous studies in midlatitude cirrus [*Heymsfield*, 2003b]. However, for the small-particle mode, previously obtained relationships do not hold. Despite the considerable variability of the size distribution parameters depending on cirrus category, such diagnostic relationships could be exploited to better account for varying shapes of cirrus PSD in bulk microphysical parameterizations and the effect on parameterized ice sedimentation rates in GCMs.

Despite striking contrasts in the PDFs of cirrus IWC and ice number concentrations for different large-scale environments, PDFs of vertical velocity are virtually the same. This lack of a dynamical contrast on smaller scales suggests that PDFs of vertical velocities are a poor predictor for explaining the microphysical variability in cirrus among various dynamical regimes. Similar PDFs of vertical velocity can be the result of different partitioning of kinetic energy between gravity wave modes and turbulence or embedded convection on small scales. This result suggests that the use of PDFs of vertical velocities in GCM cloud parameterizations may not be enough to predict or constrain the microphysical variability of cirrus clouds. It also suggests that variability in ice supersaturation and aerosols and their potential impacts on the availability of ice nuclei rather than variability in vertical velocity may be the primary drivers of the microphysical variability of midlatitude cirrus which highlights the increased need for detailed aerosol measurements in future campaigns.

Acknowledgments

Andreas Muhlbauer and Thomas P. Ackerman acknowledge funding received by the National Science Foundation (NSF) under grant 1144017. This publication is partially funded by the Joint Institute for the Study of the Atmosphere and Ocean (JISAO) under NOAA Cooperative Agreement NA10OAR4320148, Contribution 2138. Jennifer Comstock was supported by the Department of Energy (DOE) Atmospheric Measurement Program. We thank Ann M. Fridlind (NASA-GISS) for stimulating discussions on an earlier version of the manuscript and highly appreciate comments and suggestions from three anonymous reviewers that helped to improve the clarity and presentation of the manuscript.

References

Ackerman, T. P., K. N. Liou, F. P. J. Valero, and L. Pfister (1988), Heating rates in tropical anvils, *J. Atmos. Sci.*, *45*(10), 1606–1623.

Berry, E., and G. G. Mace (2013), Cirrus cloud properties and the large-scale meteorological environment: Relationships derived from A-Train and NCEP-NCAR Reanalysis data, *J. Appl. Meteorol. Climatol.*, *52*(5), 1253–1276.

Clothiaux, E. E., T. P. Ackerman, G. G. Mace, K. P. Moran, R. T. Marchand, M. A. Miller, and B. E. Martner (2000), Objective determination of cloud heights and radar reflectivities using a combination of active remote sensors at the ARM CART sites, *J. Appl. Meteorol.*, *39*(5), 645–665.

Dee, D. P., et al. (2011), The ERA-Interim reanalysis: Configuration and performance of the data assimilation system, *Q. J. R. Meteorol. Soc.*, *137*(656), 553–597.

Deng, M., G. G. Mace, Z. Wang, and R. P. Lawson (2013), Evaluation of several A-Train ice cloud retrieval products with in situ measurements collected during the SPARTICUS campaign, *J. Appl. Meteorol. Climatol.*, *52*, 1014–1030.

Eixmann, R., D. H. W. Peters, C. Zuelicke, M. Gerding, and A. Doernbrack (2010), On the upper tropospheric formation and occurrence of high and thin cirrus clouds during anticyclonic poleward Rossby wave breaking events, *Tellus*, *62*(3), 228–242.

Evans, S. M., R. T. Marchand, T. P. Ackerman, and N. Beagley (2012), Identification and analysis of atmospheric states and associated cloud properties for Darwin, australia, *J. Geophys. Res.*, *117*, D06204, doi:10.1029/2011JD017010.

Gao, R. S., et al. (2004), Evidence that nitric acid increases relative humidity in low-temperature cirrus clouds, *Science*, *303*(516), 516–520.

Garrett, T. J., A. J. Heymsfield, M. J. McGill, B. A. Ridley, D. G. Baumgardner, T. P. Bui, and C. R. Webster (2004), Convective generation of cirrus near the tropopause, *J. Geophys. Res.*, *109*, D21203, doi:10.1029/2004JD004952.

Gettelman, A., X. Liu, S. J. Ghan, H. Morrison, S. Park, A. J. Conley, S. A. Klein, J. Boyle, D. L. Mitchell, and J. L. F. Li (2010), Global simulations of ice nucleation and ice supersaturation with an improved cloud scheme in the Community Atmosphere model, *J. Geophys. Res.*, *115*, D18216, doi:10.1029/2009JD013797.

Gultepe, I., and D. O. Starr (1995), Dynamical structure and turbulence in cirrus clouds: Aircraft observations during FIRE, *J. Atmos. Sci.*, *52*(23), 4159–4181.

Gultepe, I., A. J. Heymsfield, and D. H. Lenschow (1990), A comparison of vertical velocity in cirrus obtained from aircraft and lidar divergence measurements during fire, *J. Atmos. Oceanic Technol.*, *7*(1), 58–67.

Gultepe, I., D. O. Starr, A. J. Heymsfield, T. Uttal, T. P. Ackerman, and D. L. Westphal (1995), Dynamical characteristics of cirrus clouds from aircraft and radar observations in micro and meso-γ scales, *J. Atmos. Sci.*, *52*(23), 4060–4078.

Heymsfield, A. J. (2003a), Properties of tropical and midlatitude ice cloud particle ensembles. Part I: Median mass diameters and terminal velocities, *J. Atmos. Sci.*, *60*(21), 2573–2591.

Heymsfield, A. J. (2003b), Properties of tropical and midlatitude ice cloud particle ensembles. Part II: Applications for mesoscale and climate models, *J. Atmos. Sci.*, *60*(21), 2592–2611.

Heymsfield, A. J., A. Bansemer, P. R. Field, S. L. Durden, J. L. Stith, J. E. Dye, W. Hall, and C. A. Grainger (2002), Observations and parameterizations of particle size distributions in deep tropical cirrus and stratiform precipitating clouds: Results from in situ observations in TRMM field campaigns, *J. Atmos. Sci.*, *59*(24), 3457–3491.

Ivanova, D., D. L. Mitchell, W. P. Arnott, and M. Poellot (2001), A GCM parameterization for bimodal size spectra and ice mass removal rates in mid-latitude cirrus clouds, *Atmos. Res.*, *59*, 89–113.

Jackson, R. C., G. M. McFarquhar, A. V. Korolev, M. E. Earle, P. S. K. Liu, R. P. Lawson, S. Brooks, M. Wolde, A. Laskin, and M. Freer (2012), The dependence of ice microphysics on aerosol concentration in arctic mixed-phase stratus clouds during ISDAC and m-pace, *J. Geophys. Res.*, *117*, D15207, doi:10.1029/2012JD017668.

Jensen, E., et al. (2009), On the importance of small ice crystals in tropical anvil cirrus, *Atmos. Chem. Phys.*, *9*(15), 5519–5537.

Jensen, E. J., R. P. Lawson, J. W. Bergman, L. Pfister, T. P. Bui, and C. G. Schmitt (2013), Physical processes controlling ice concentrations in synoptically forced, midlatitude cirrus, *J. Geophys. Res. Atmos.*, *118*, 5348–5360, doi:10.1002/jgrd.50421.

Joos, H., P. Spichtinger, U. Lohmann, J. F. Gayet, and A. Minikin (2008), Orographic cirrus in the global climate model echam5, *J. Geophys. Res.*, *113*, D18205, doi:10.1029/2007JD009605.

Kalesse, H., and P. Kollias (2013), Climatology of high cloud dynamics using profiling ARM Doppler radar observations, *J. Clim.*, *26*, 6340–6359, doi:10.1175/JCLI–D–12–00695.1.

Karcher, B., and J. Strom (2003), The roles of dynamical variability and aerosols in cirrus cloud formation, *Atmos. Chem. Phys.*, *3*, 823–838.

Koop, T., B. P. Luo, A. Tsias, and T. Peter (2000), Water activity as the determinant for homogeneous ice nucleation in aqueous solutions, *Nature*, *406*(6796), 611–614.

Korolev, A. (2007), Reconstruction of the sizes of spherical particles from their shadow impages. Part I: Theoretical considerations, *J. Atmos. Oceanic Technol.*, *24*, 376–389.

Korolev, A., and G. A. Isaac (2005), Shattering during sampling by OAPs and HVPS. Part I: Snow particles, *J. Atmos. Oceanic Technol.*, *22*(5), 528–542.

Korolev, A. V., E. F. Emery, J. W. Strapp, S. G. Cober, G. A. Isaac, M. Wasey, and D. Marcotte (2011), Small ice particles in tropospheric clouds: Fact or artifact? Airborne icing instrumentation evaluation experiment, *Bull. Am. Meteorol. Soc.*, *92*(8), 967–973.

Kozu, T., and K. Nakamura (1991), Rainfall parameter-estimation from dual-radar measurements combining reflectivity profile and path-integrated attenuation, *J. Atmos. Oceanic Technol.*, *8*(2), 259–270.

Kraemer, M., et al. (2009), Ice supersaturations and cirrus cloud crystal numbers, *Atmos. Chem. Phys.*, *9*(11), 3505–3522.

Lawson, R. P. (2011), Effects of ice particles shattering on the 2D-S probe, *Atmos. Meas. Tech.*, *4*(7), 1361–1381.

Lawson, R. P., L. J. Angus, and A. J. Heymsfield (1998), Cloud particle measurements in thunderstorm anvils and possible weather threat to aviation, *J. Aircr.*, *35*(1), 113–121.

Lawson, R. P., D. O'Connor, P. Zmarzly, K. Weaver, B. Baker, and Q. Mo (2006), The 2D-S (Stereo) probe: Design and preliminary tests of a new airborne, high-speed, high-resolution particle imaging probe, *J. Atmos. Oceanic Technol.*, *23*(11), 1462–1477.

Lawson, R. P., E. Jensen, D. L. Mitchell, B. Baker, Q. Mo, and B. Pilson (2010), Microphysical and radiative properties of tropical clouds investigated in tc4 and namma, *J. Geophys. Res.*, *115*, D00J08, doi:10.1029/2009JD013017.

Lenschow, D. H. (1972), The measurement of air velocity and temperature using the NCAR Buffalo Aircraft Measuring System, *Tech. Rep.*, Natl. Cent. for Atmos. Res., Boulder, Colo.

Liu, X., J. E. Penner, S. J. Ghan, and M. Wang (2007), Inclusion of ice microphysics in the NCAR community atmospheric model version 3 (cam3), *J. Clim.*, *20*(18), 4526–4547.

Mace, G. G., D. O. Starr, T. P. Ackerman, and P. Minnis (1995), Examination of coupling between an upper-tropospheric cloud system and synoptic-scale dynamics diagnosed from wind profiler and radiosonde data, *J. Atmos. Sci.*, *52*(23), 4094–4127.

Mace, G. G., T. P. Ackerman, E. E. Clothiaux, and B. A. Albrecht (1997), A study of composite citrus morphology using data from a 94-GHz radar and correlations with temperature and large-scale vertical motion, *J. Geophys. Res.*, *102*(D12), 13,581–13,593.

Mace, G. G., E. E. Clothiaux, and T. P. Ackerman (2001), The composite characteristics of cirrus clouds: Bulk properties revealed by one year of continuous cloud radar data, *J. Clim.*, *14*(10), 2185–2203.

Mace, G. G., S. Benson, and E. Vernon (2006), Cirrus clouds and the large-scale atmospheric state: Relationships revealed by six years of ground-based data, *J. Clim.*, *19*(13), 3257–3278.

Marchand, R., N. Beagley, S. E. Thompson, T. P. Ackerman, and D. M. Schultz (2006), A bootstrap technique for testing the relationship between local-scale radar observations of cloud occurrence and large-scale atmospheric fields, *J. Atmos. Sci.*, *63*(11), 2813–2830.

Marchand, R., N. Beagley, and T. P. Ackerman (2009), Evaluation of hydrometeor occurrence profiles in the multiscale modeling framework climate model using atmospheric classification, *J. Clim.*, *22*(17), 4557–4573.

McFarquhar, G. M., J. Um, M. Freer, D. Baumgardner, G. L. Kok, and G. Mace (2007), Importance of small ice crystals to cirrus properties: Observations from the Tropical Warm Pool International Cloud Experiment (TWP-ICE), *Geophys. Res. Lett.*, *34*, L13803, doi:10.1029/2007GL029865.

Mitchell, D. L. (1991), Evolution of snow-size spectra in cyclonic storms. 2. Deviations from the exponential form, *J. Atmos. Sci.*, *48*(16), 1885–1899.

Mitchell, D. L., P. Rasch, D. Ivanova, G. McFarquhar, and T. Nousiainen (2008), Impact of small ice crystal assumptions on ice sedimentation rates in cirrus clouds and GCM simulations, *Geophys. Res. Lett.*, *35*, L09806, doi:10.1029/2008GL033552.

Mitchell, D. L., S. Mishra, and R. P. Lawson (2011), Representing the ice fall speed in climate models: Results from Tropical Composition, Cloud and Climate Coupling (TC4) and the Indirect and Semi-Direct Aerosol Campaign (ISDAC), *J. Geophys. Res.*, *116*, D00T03, doi:10.1029/2010JD015433.

Muelmenstaedt, J., D. Lubin, L. M. Russell, and A. M. Vogelmann (2012), Cloud properties over the North Slope of Alaska: Identifying the prevailing meteorological regimes, *J. Clim.*, *25*(23), 8238–8258.

Murphy, D. M., and T. Koop (2005), Review of the vapour pressure of ice and supercooled water for atmospheric applications, *Q. J. R. Meteorol. Soc.*, *131*, 1539–1565.

Quante, M. (2006), Turbulenz in Cirruswolken mittlerer Breite, Ph.D. thesis, Universität Hamburg, 168 pp.

Sanderson, B. M., C. Piani, W. Ingram, D. A. Stone, and M. R. Allen (2008), Towards constraining climate sensitivity by linear analysis of feedback patterns in thousands of perturbed-physics GCM simulations, *Clim. Dyn.*, *30*(2–3), 175–190.

Sassen, K. (1997), Cirrus clouds: A modern perspective, in *Cirrus*, edited by D. Lynch, pp. 11–40, Oxford Univ. Press, New York.

Sassen, K., and J. R. Campbell (2001), A midlatitude cirrus cloud climatology from the facility for atmospheric remote sensing. Part I: Macrophysical and synoptic properties, *J. Atmos. Sci.*, *58*(5), 481–496.

Sassen, K., Z. Wang, and D. Liu (2008), Global distribution of cirrus clouds from CloudSat/Cloud-Aerosol Lidar and Infrared Pathfinder Satellite Observations (CALIPSO) measurements, *J. Geophys. Res.*, *113*, D00A12, doi:10.1029/2008JD009972.

Saw, E.-W., J. P. L. C. Salazar, L. R. Collins, and R. A. Shaw (2012a), Spatial clustering of polydisperse inertial particles in turbulence: I. Comparing simulation with theory, *New J. Phys.*, *14*, 105030, doi:10.1088/1367–2630/14/10/105031.

Saw, E.-W., R. A. Shaw, J. P. L. C. Salazar, and L. R. Collins (2012b), Spatial clustering of polydisperse inertial particles in turbulence: II. Comparing simulation with experiment, *New J. Phys.*, *14*, 105031, doi:10.1088/1367–2630/14/10/105031.

Spichtinger, P., K. Gierens, and H. Wernli (2005a), A case study on the formation and evolution of ice supersaturation in the vicinity of a warm conveyor belt's outflow region, *Atmos. Chem. Phys.*, *5*, 973–987.

Spichtinger, P., K. Gierens, and A. Dornbrack (2005b), Formation of ice supersaturation by mesoscale gravity waves, *Atmos. Chem. Phys.*, *5*, 1243–1255.

Stubenrauch, C. J., A. Chedin, G. Radel, N. A. Scott, and S. Serrar (2006), Cloud properties and their seasonal and diurnal variability from TOVS path-B, *J. Clim.*, *19*(21), 5531–5553.

Zelinka, M. D., S. A. Klein, and D. L. Hartmann (2012), Computing and partitioning cloud feedbacks using cloud property histograms. Part I: Cloud radiative kernels, *J. Clim.*, *25*(11), 3715–3735.

Zhang, K., X. Liu, M. Wang, J. M. Comstock, D. L. Mitchell, S. Mishra, and G. G. Mace (2013), Evaluating and constraining ice cloud parameterizations in cam5 using aircraft measurements from the sparticus campaign, *Atmos. Chem. Phys.*, *13*, 4963–4982.

Zhao, Y., G. G. Mace, and J. M. Comstock (2011), The occurrence of particle size distribution bimodality in midlatitude cirrus as inferred from ground-based remote sensing data, *J. Atmos. Sci.*, *68*(6), 1162–1177.